Comptes Rendus

Géoscience

Sciences de la Planète

Fateh Bouchaala, Mohammed Y. Ali and Jun Matsushima

Compressional and shear wave attenuations from walkway VSP and sonic data in an offshore Abu Dhabi oilfield

Original Article — Internal Geophysics

Compressional and shear wave attenuations from walkway VSP and sonic data in an offshore Abu Dhabi oilfield

Fateh Bouchaala [*, a], **Mohammed Y. Ali** [a] **and Jun Matsushima** [b]

[a] Department of Earth Sciences, Khalifa University, P O Box 127788, Abu Dhabi, UAE

[b] Department of Environment Systems, the University of Tokyo, Tokyo, Japan

E-mails: fateh.bouchaala@ku.ac.ae (F. Bouchaala), mohammed.ali@ku.ac.ae
(M. Y. Ali), jun-matsushima@edu.k.u-tokyo.ac.jp (J. Matsushima)

Abstract. Seismic attenuation was estimated from compressional (P) and shear (S) waves carefully extracted from three-component vertical seismic profiling (VSP) data. A high sensitivity of attenuation to fluid content was noticed, which shows the advantage of its use as a seismic attribute for reservoir studies. Contrary to most observations in fully saturated sandstones, the magnitude of P to S wave attenuation in the studied carbonate reservoir zones is higher than one. This disagreement is most probably because the fluid flow models developed to describe the attenuation mechanisms in sandstones are not valid for carbonate rocks due their complex texture. Moreover, the magnitude of seismic attenuation in the reservoir zones is controlled by the saturation of pore fluids and clay content. Furthermore, the attenuation magnitudes obtained at sonic and VSP frequencies are of the same order, and compressional and shear attenuations show similar variation at both frequencies. This indicates frequency-independent attenuations in the studied oilfield.

Keywords. Attenuation, Reservoir, Three-component rotation, VSP, Sonic.

Manuscript received 12th March 2021, revised 15th June 2021 and 30th July 2021, accepted 10th September 2021.

1. Introduction

Seismic wave attenuation illustrates the energy losses during wave propagation and is often quantified through the inverse of the quality factor, *Q*. The energy losses are mainly the result of scattering and fluid-related mechanisms. Scattering describes the losses due to multiple small reflections caused by the heterogeneities of the subsurface [Wu and Aki,

1988], while fluid-related mechanisms such as wave-induce fluid flow (WIFF) describes the energy losses due to the frictional movement between solid grains and pore fluids [e.g., Murphy et al., 1986, Müller et al., 2010]. Thereby, seismic attenuation might be an efficient seismic attribute for studying heterogeneous and fractured media such as carbonate reservoirs. Indeed, several attenuation studies have been successfully conducted with applications in the petroleum industry [e.g., Bouchaala and Guennou, 2012, Matsushima et al., 2018], seismology [e.g., Del Pezzo et al., 2019, Prudencio et al., 2013], and

civil engineering [e.g., Boadu, 1997, Li et al., 2018]. Mavko and Nur [1979], who developed one of the earliest models describing seismic wave attenuation in saturated rocks, reported a strong increase in attenuation induced by a small amount of free gas. Several subsequent studies investigated attenuation in partially saturated media [e.g., Bouchaala and Guennou, 2012, Müller et al., 2010], and most of them confirmed the strong magnitude of attenuation as observed by Mavko and Nur [1979]. Moreover, the direct link between fluid viscosity and attenuation allowed Shabelansky et al. [2015] to use the latter as a proxy to monitor the viscosity changes during the heating of heavy oil reservoirs, and hence to manage the production.

The combination of compressional (Q_P^{-1}) and shear (Q_S^{-1}) attenuations can help to enhance reservoir characterization by allowing more reservoir properties to be obtained than by the use of a unique attenuation mode. Winkler and Nur [1982] observed that the magnitude of the attenuation ratio Q_S/Q_P is higher than 1 in partially saturated rocks and less than 1 in fully saturated rocks. They also noticed that the attenuation ratio is more sensitive to the presence of the gas than the velocity ratio. Klimentos [1995] noticed $Q_S/Q_P > 1$ in rocks containing gas or condensate, and the opposite in rocks fully saturated with water or with water and oil. Hence, the attenuation ratio Q_S/Q_P may help to distinguish between gas and condensate from oil and water. Qi et al. [2017] also estimated Q_P^{-1} and Q_S^{-1} from sonic waveforms and suggested that the magnitude of Q_S/Q_P is largely controlled by gas saturation.

Even though the use of S wave attenuation may be largely useful for reservoir characterization, the difficulty of its extraction from field data makes the most in situ attenuation studies to be based on only P waves. The high heterogeneous nature of carbonate rocks increases the difficulties of the extraction of shear waves. The few seismic in situ attenuation studies carried out in carbonates rocks were mainly based on P waves [e.g., Bouchaala et al., 2016b, 2014]. The S wave attenuation in carbonate rocks is usually estimated either from sonic waveforms [e.g., Bouchaala et al., 2019a, Matsushima et al., 2018] or in laboratory at ultrasonic frequencies [e.g., Adam et al., 2009, Assefa et al., 1999], because in both cases S waves are generated and recorded separately from P waves. Bouchaala et al. [2016a] studied the attenu-

ation of a carbonate reservoir in Abu Dhabi. They noticed a high dispersion of the values of the fast and slow sonic shear waves ratio (Q_{S_2}/Q_{S_1}) with depth in highly fractured zones, and small dispersion in slightly fractured zones. Adam et al. [2009] calculated Q_P^{-1} and Q_S^{-1} from five carbonate samples with different petrophysical properties. Curiously and in contrast to most of sandstone observations, they found that $Q_S/Q_P > 1$ in dry and fully saturated media, and $Q_S/Q_P < 1$ in partially saturated media. They also reported a compressional attenuation increase of 250% after the substitution of brine by light hydrocarbon in the samples. Therefore, including shear waves in the in situ attenuation studies of Abu Dhabi carbonate reservoirs may help in providing clear-sightedness on the magnitude of Q_S/Q_P and its dependence on petrophysical properties of the reservoir zones.

The aim of this study is to estimate attenuation from downgoing P and S waves that are properly extracted from three-component (3C) vertical seismic profiling (VSP) data acquired over an offshore Abu Dhabi oilfield. For a proper extraction of P and S waves, the 3C raw VSP data were carefully processed by trying to preserve the amplitudes as much as possible, then rotated in order to maximize the shear energy. After that, wavefields were separated to produce four independent wavefields: downgoing P, downgoing S, upgoing P, and upgoing S. We applied the spectral ratio method [Bath, 1974, McDonal et al., 1958] to estimate Q_P and Q_S from the downgoing waveforms. Furthermore, we estimated compressional and shear sonic attenuations, which permits the investigation of frequency dependence of attenuation.

2. Study area and field data

The oilfield is an east–west plunging anticline, located in offshore Abu Dhabi, United Arab Emirates (UAE). The oilfield is characterized by gentle dips with steepest dips occurring in the north and northeast where the average dip is about 2.5°. The stratigraphy of the oilfield is mostly made of carbonates of Mesozoic–Cenozoic in age. The reservoir zones are made of stacked sections of porous, shallow water carbonates of the Lower Cretaceous Thamama Group. The studied reservoirs are divided into three zones: TH1, TH2, and TH3. The average reservoir porosity ranges from 10 to 25% and the permeability from 10 to 100 md. Fractures have been reported
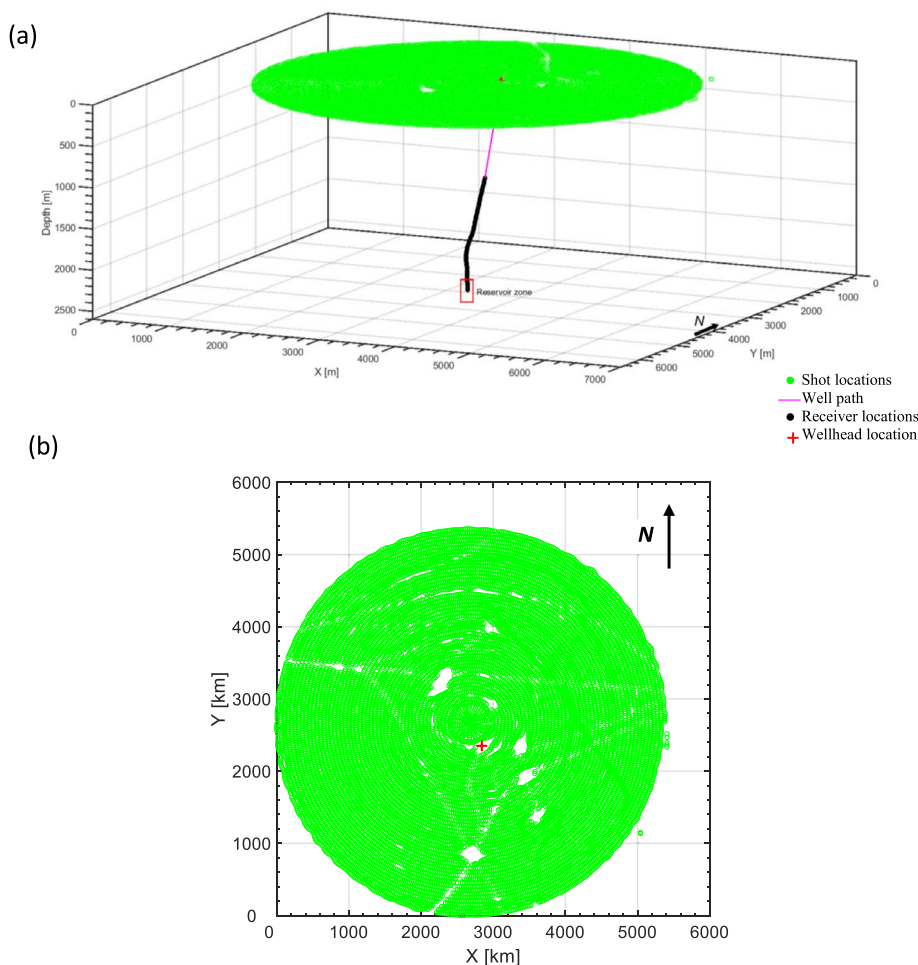
Figure 1. (a) The acquisition geometry of 3D VSP data acquired with seventy receivers placed 20 m apart [modified from Bouchaala et al., 2019b]. (b) Map view of shot locations.

in TH1 and TH3 [Edwards et al., 2006, Skeith et al., 2015]. These fractures generally occur at the boundaries of dense zones and reservoir units [Shekhar et al., 2017].

The 3C 3D VSP data were acquired with a maximum source offset of 3000 m from the wellhead. Seventy receivers were placed 20 m apart in the wellbore to record the data generated by 18047 shots with average shot spacing of 25 m (Figure 1). Due to weather conditions and obstacles such as platforms, the survey geometry was not shot regularly as originally planned, though its coverage is very good. The extracted shots at near (200 m), middle (1050 m), and far (2500 m) offsets (Figure 2) show that the overall data quality is good except at far offset, in the

depth range of 1145–1525 m (receivers 1–20) and at the depth of 1705 m (receiver 29). Furthermore, receiver 60 at the depth of 2325 m did not record any data (Figure 2).

The relative bearing (RB) technique [e.g., Armstrong, 2005, Kazemi and Naville, 2017] was applied to rotate the data from the local reference frame to the geographic coordinate system (north–south, east–west, and true vertical). The RB angles were recorded by the RB sensor, which is a weighted potentiometer, located between the X and Y receivers. As the tool tilts in a deviated well, the RB sensor measures the position of the X axis relative to the well azimuth. The RB angles were used along with the azimuths of the well deviation to orient the receivers in
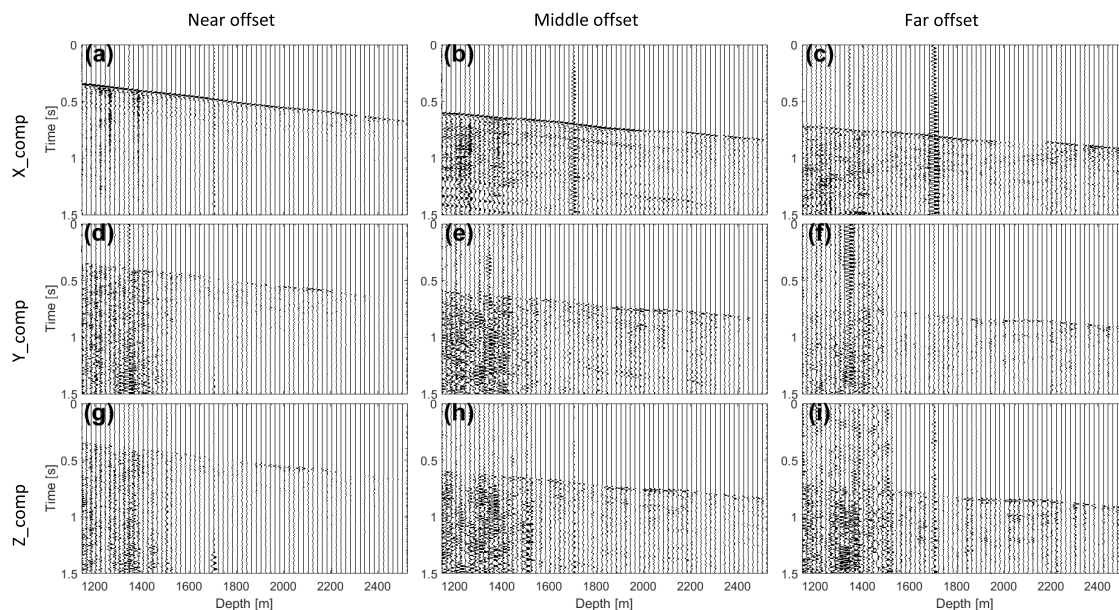
Figure 2. Vertical Z (a, b, c), horizontal X (d, e, f) and Y (g, h, i) components of raw VSP data recorded at near offset (a, d, g), middle offset (b, e, h) and far offset (c, f, i).

the geographic coordinate system. Furthermore, the anomalous amplitude attenuation (AAA) processing was applied in order to reduce the random noise and abnormal spikes in the data. The AAA technique transforms the data into the frequency domain and applies a spatial median filter [e.g., Guo and Lin, 2003, Wu et al., 2017]. Then, the Wavesip method [Leaney, 2002] was used to decompose the 3C component data into P, Sv upgoing, and downgoing wavefields (Figure 3). In this method, the slowness and the polarization of each plane wave are calculated. Then, a linear system is solved in the frequency domain in order to compute plane-wave amplitudes. Finally, a summation by wave types (downgoing P, downgoing Sv, upgoing P, and upgoing Sv) is performed over the plane waves to separate the wavefields. The noisy data and dead traces were not used in the wavefield separation. The Wavesip method can handle anisotropic media and it can preserve the amplitudes, which permits the use of the decomposed wavefields for AVO analysis, prestack migration, and attenuation analysis [Graves et al., 2008, Leaney, 2002]. Furthermore, this method is well appropriate for 3D VSP data acquired with large receiver array [Leaney, 2002]. More details about the Wavesip method are provided in Appendix A.

Sonic data were also acquired in the reservoir zones during the VSP experiment by using a high-resolution (0.1524 m) dipole sonic imager (DSI) (Figure 15). The DSI tool allows a separate acquisition of compressional monopole (mo) and shear dipole (xd) waveforms. However, due to a limitation in data quality, we only used the sonic waveforms recorded in the depth range of 2294–2389 m (Figure 4), which covers the reservoir zone TH1 and the uppermost part of the reservoir zone TH2. The high resolution of sonic waveforms allows a direct comparison between the attenuation and the other petrophysical logs recorded with the same resolution.

3. Estimation of VSP attenuation

We generated receiver gathers from downgoing P and S wavefields of shots that have azimuths close to the north–south direction with an accuracy of ±5° (Figure 5a). After a meticulous analysis of the receiver gathers of downgoing waves, we noticed that the seismic event indicated by red curves in Figures 5b–d, has a good signal to noise ratio (SNR) in most of receivers with the highest SNR at the offset range of 817–1218 m. Therefore, we selected this seismic event at these offsets for the estimation of
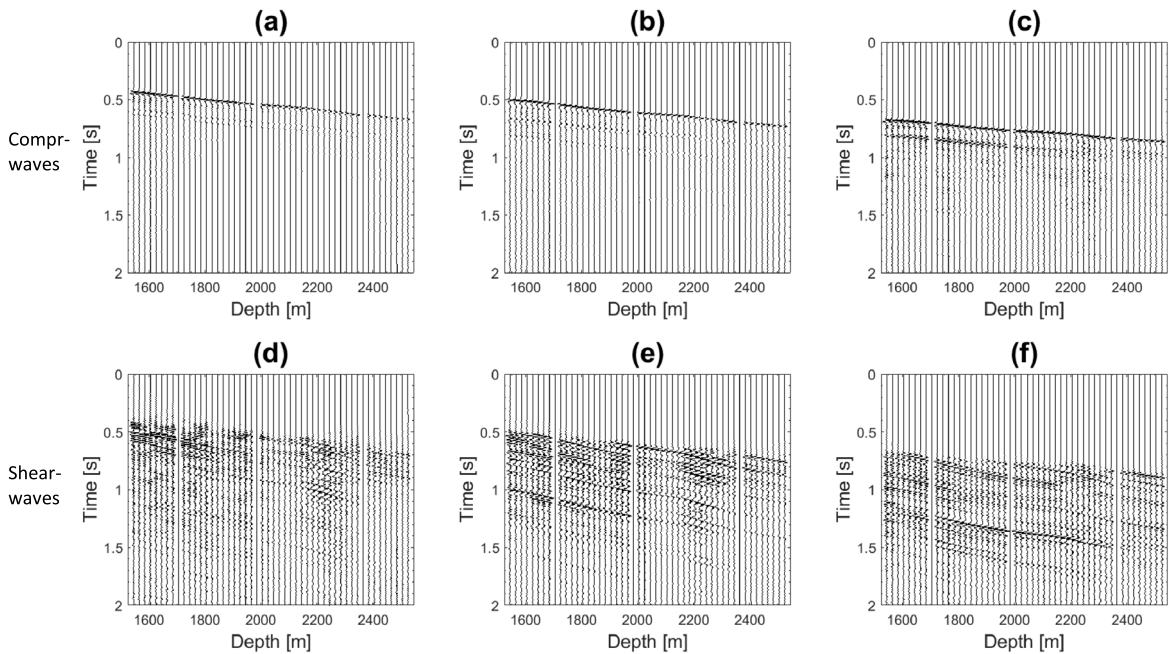
Figure 3. Separated compressional (a, b, c) and shear (d, e, f) wavefields at near offset (a, d), middle offset (b, e) and far offset (c, f).
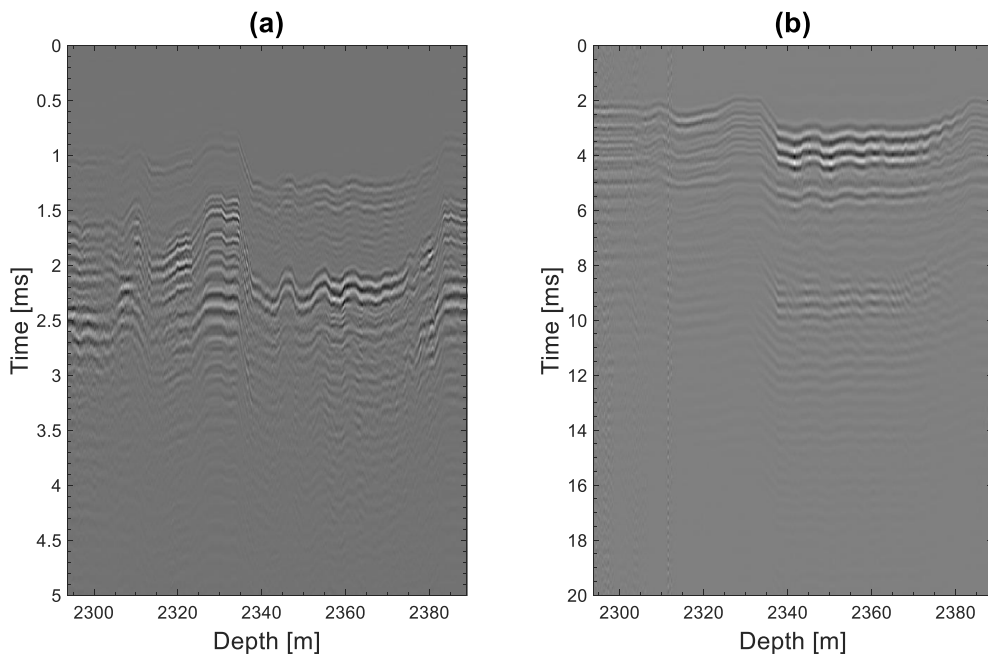

Figure 4. Monopole (mo) and dipole (xd) waveforms recorded at one of the DSI receivers in the reservoir zones.
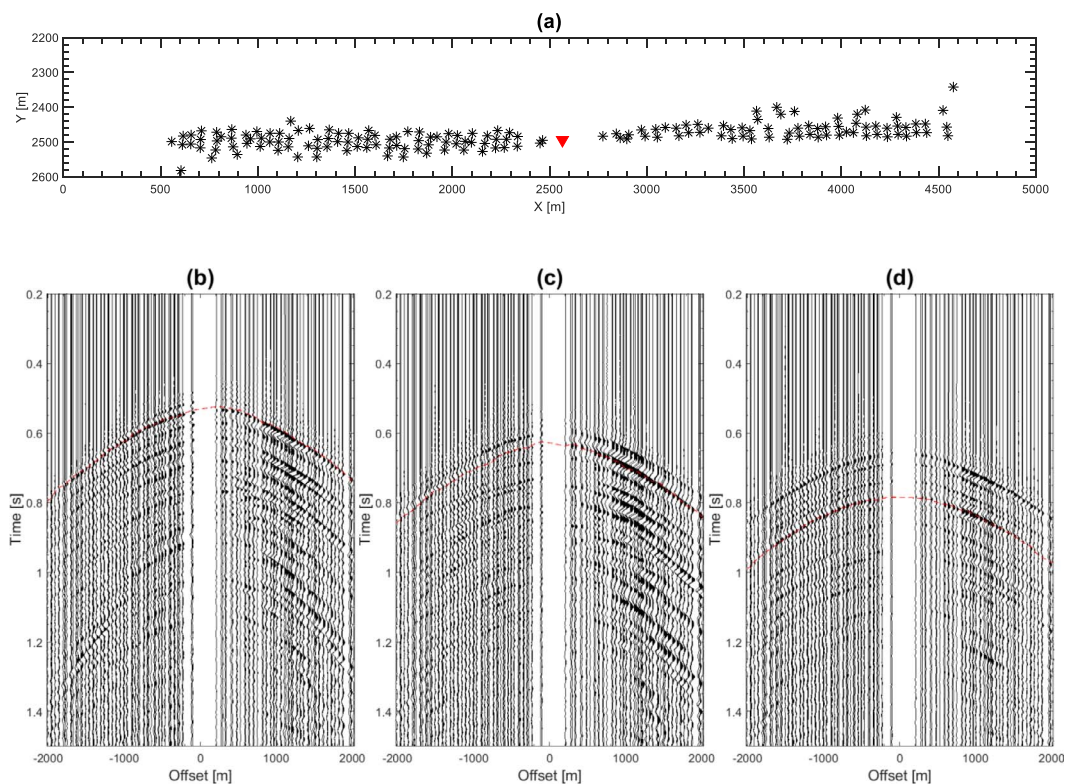
Figure 5. (a) Map view of the selected shots for the attenuation study. The shots are lined up along the north–south direction with an accuracy of ±5°. The red triangle indicates the VSP wellhead. (b, c, d) Receiver gathers of downgoing S waves at depths of 1925 m, 2185 m, and 2305 m, respectively. The dashed red curves indicate waveforms generated from P waves converted at the top of Fiqa Formation from which shear wave attenuation was estimated.

S attenuation. Based on the simulated travel time of downgoing S waves, calculated by using a 1D sonic log (Figure 6), we suggest that the selected downgoing event is generated from a P conversion close to the top of the Upper Cretaceous Fiqa Formation, which is dominated by argillaceous limestone and calcareous shales [Ali and Farid, 2016]. In order to confirm the shear mode of the selected seismic event, we extracted portion of waveforms already rotated to geographic coordinates system by using a Hanning window of 90 ms length, centered at the travel times indicated by red curves in Figures 5b–d. Then, we rotated the extracted waveforms to produce ray-based coordinate system of L, Q, and T waveforms which are aligned in the direction of P, SV, and SH phase motions, respectively. Figure 7 shows that Q waveform has the strongest particle

motion, while T has the weakest particle motion. This demonstrates the strong presence of P to SV converted waveforms at the travel times indicated by red curves in Figures 5b–d.

We aligned traces recorded in the offset range of 817–1218 m by using the simulated travel times. Then, an automatic picking of amplitude maxima was performed to refine the alignment, before stacking the traces in order to increase the SNR and hence, to facilitate the extraction of the downgoing S waves. A Hanning window with a length of 70 ms was chosen to extract the S waves (Figure 8a). In addition to S waves, we also extracted the first arrival of downgoing P waves, which are easily identifiable by their high amplitudes (Figures 3a–c). A Hanning window with a length of 60 ms was used to extract P waves (Figure 8b).
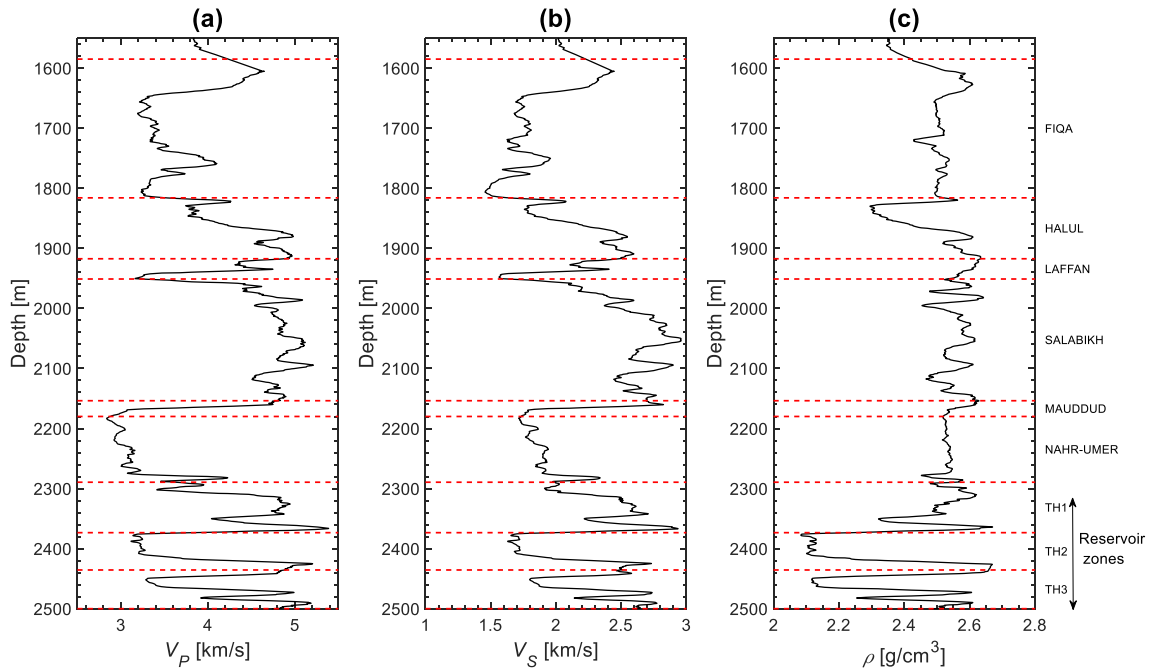
Figure 6. Smoothed version of (a) compressional sonic log, (b) shear sonic log, and (c) density log. The dashed horizontal lines and the text labels indicate the tops and names of the various geological formations, respectively.
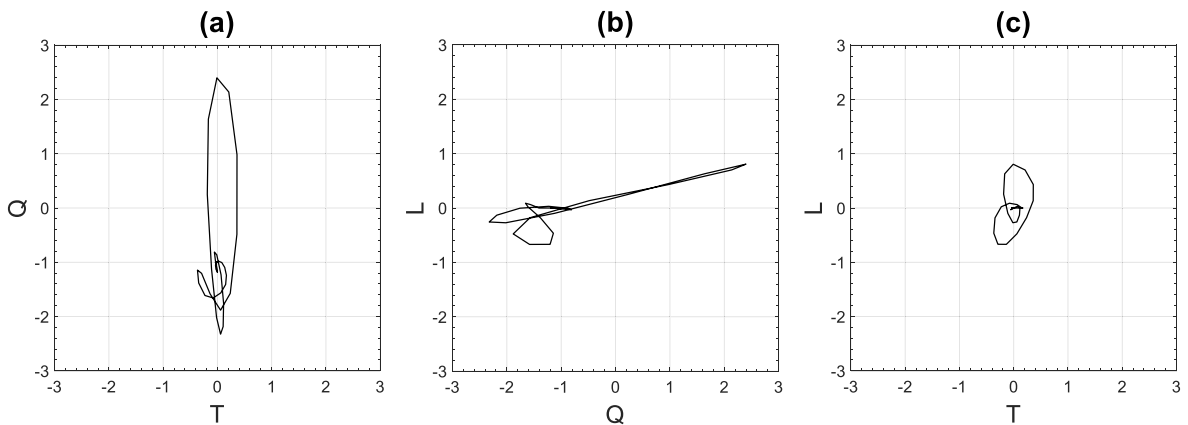

Figure 7. Particle motion of waveforms extracted around the time indicated by the dashed curves in Figure 5. The waveforms are aligned in the direction of L, Q, and T, the components of a ray-based coordinate system which are aligned with P, SV, and SH phase motions. The waveforms are recorded at a depth of 2305 m and an offset of 972 m.

We estimated seismic wave attenuation in each formation by using the extracted waveforms of each two receivers located at the top and the bottom of each formation and reservoir zones. The spectral ratio method [Bath, 1974, McDonal et al., 1958] was applied to estimate seismic wave attenuation from the extracted downgoing waves. In this method, a linear regression is performed between
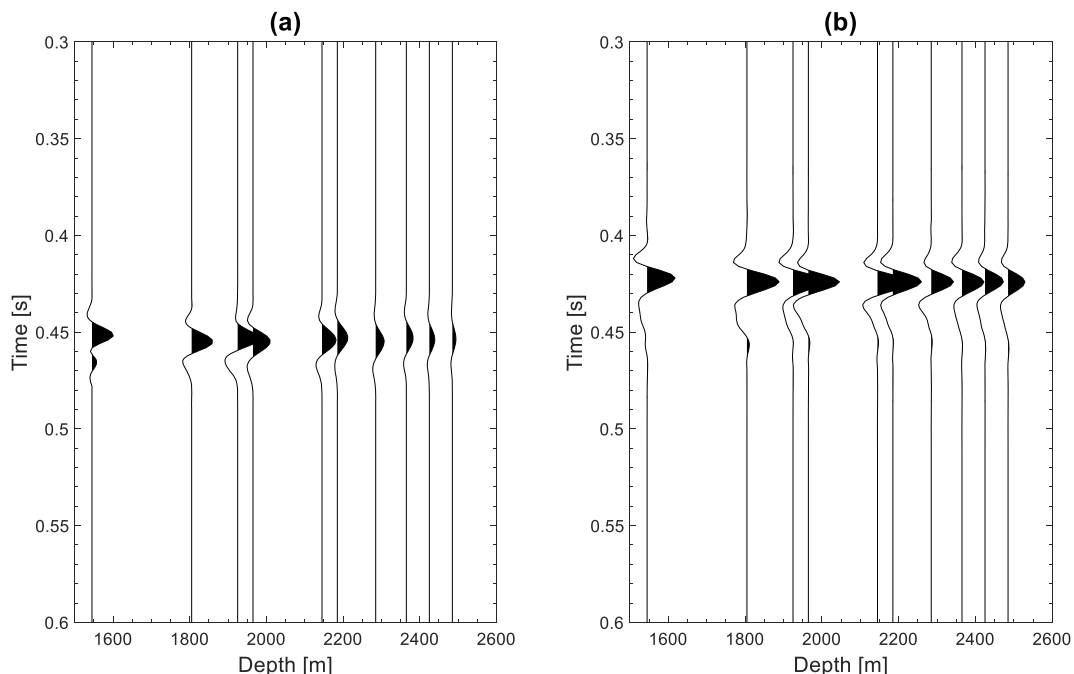
(a)

(b)

Figure 8. (a) Stacked S waveforms and (b) P waveforms recorded in the offset range of 817–1218 m at the top and bottom of each formation and reservoir zones. The P and S waveforms were extracted by using a Hann window of 60 ms and 70 ms, respectively.

the logarithmic ratio in the left-hand side of (1) and frequency f.

$$\ln\left[\frac{S(z_2, f)}{S(z_1, f)}\right] = w + mf, \qquad (1)$$

where $S(z_1, f)$ and $S(z_2, f)$ are the amplitude spectra of two waves recorded at two different depths z_1 and z_2 ($z_2 > z_1$), and w is a frequency-independent constant. Their arrivals are shifted by the time Δt. Seismic wave attenuation (Q^{-1}) is calculated from the slope m of the linear regression defined as follows:

$$m = -\pi \Delta t Q^{-1} \qquad (2)$$

In the spectral ratio (SR) method, calculations based on the two spectra should account for ray path geometry to properly attribute the attenuation to a specific position or layer. This is obviously easier in zero-offset data, but this is not a strict requirement, especially when there is a small lateral velocity variation as the case of the oilfield of this study [Takougang et al., 2020]. Bouchaala et al. [2019b] critically discussed the effect of the offset on the accuracy of the spectral ratio method, by using synthetic data similar to VSP data used in the present study. They noticed

that the effect of offset on SR method is noticeable at offsets larger than 2000 m, where the trend and magnitudes of attenuation profiles start to considerably differ from the zero-offset profile. However, the trend and magnitudes of zero-offset attenuation profile are similar at offsets less than 2000 m, meaning that the obtained attenuation profiles are acceptable at least for a qualitative study, as is the case of this study.

After applying the spectral ratio method in specific intervals of the full frequency ranges, we noticed that the Q^{-1} profiles with the most reasonable magnitudes (less than 1 and mostly positive) and the best linear regression were obtained in the frequency ranges of 7–90 Hz and 5–85 Hz for P and S waves, respectively (Figures 9 and 16). The standard errors (SE) of the linear regressions are in the range of 0.0023–0.0024 and 0.0025–0.0036 for P and S waves, respectively (Figure 10a). The larger SE error magnitudes of S waves was expected because of the difficulty in extracting S waveforms compared to P waveforms. The Q_P^{-1} magnitudes vary from −0.034 to 0.135 (Figure 10b), while the Q_S^{-1} magnitudes vary from 0.015
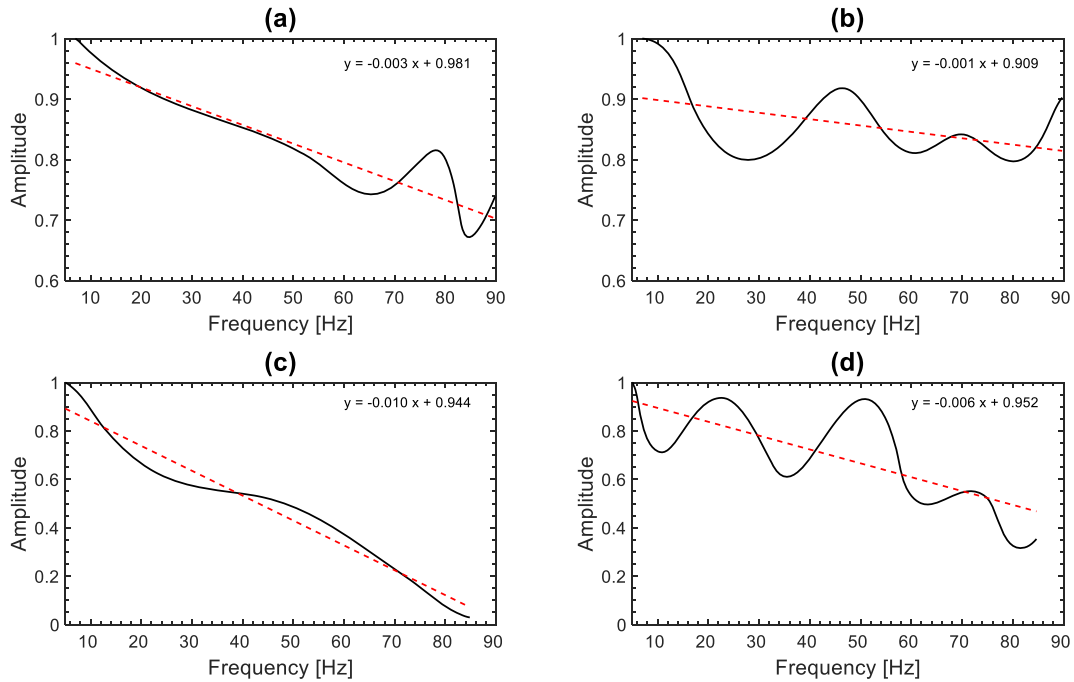
Figure 9. Curves of normalized amplitude of the spectral ratio versus frequency of the best (a, c) and the worst (b, d) linear regression for P waves (upper row) and S waves (lower row). The dashed lines represent the linear regression lines.

to 0.173 (Figure 10c). The magnitudes of Q_S^{-1} are globally larger than those of Q_P^{-1} except in the reservoir zones.

The Wasia Group, which consist of Salabikh, Mauddud, and Nahr-Umer Formations, displays the highest attenuation magnitudes. The Thamama reservoir zones (TH1, TH2, and TH3) display attenuation magnitudes lower than those of Wasia Group as in Figures 10a and c, even though these reservoir zones contain fluids and consequently attenuation is expected to be high. This is explained by the fact that the estimated attenuation is a combination of the intrinsic attenuation (Q_{in}^{-1}) and scattering (Q_{sc}^{-1}). The latter is an elastic phenomenon, which quantifies the losses due to small reflections caused by the heterogeneity of the subsurface formations. Therefore, to investigate the link between pore fluids and attenuation, Q_{sc}^{-1} component should be removed from Q^{-1}, which is usually referred to as total attenuation. Schoenberger and Levin [1974] expressed Q^{-1} as follows:

$$Q^{-1} = Q_{\text{in}}^{-1} + Q_{\text{sc}}^{-1} \tag{3}$$

Therefore, based on (3) Q_{in}^{-1} and Q_{sc}^{-1} profiles can be separately estimated by calculating Q_{sc}^{-1} first, then subtracting it from Q^{-1} to obtain Q_{in}^{-1}.

Scattering was estimated by applying the spectral ratio method on synthetic seismograms generated from the convolution of the reflectivity with a unit spike as an input source wavelet. The reflectivity of the medium was obtained by using Goupillaud model [Goupillaud, 1961], which expresses the relationship between reflected and transmitted responses at the top (R_k, T_k) and the bottom (R_{k+1}, T_{k+1}) of the kth layer as

$$\begin{Bmatrix} T_k \\ R_k \end{Bmatrix} = \frac{1}{1 + r_k} \begin{Bmatrix} e^{i\omega\tau_k} & r_k e^{i\omega\tau_k} \\ r_k e^{-i\omega\tau_k} & e^{-i\omega\tau_k} \end{Bmatrix} \begin{Bmatrix} T_{k+1} \\ R_{k+1} \end{Bmatrix}$$
$$= \{M_k\} \begin{Bmatrix} T_{k+1} \\ R_{k+1} \end{Bmatrix}, \tag{4}$$

where ω is the angular frequency, τ_k is the two-way travel time of the kth layer, and r_k is the reflection coefficient at the kth interface calculated from the smoothed sonic and density logs (Figure 6).
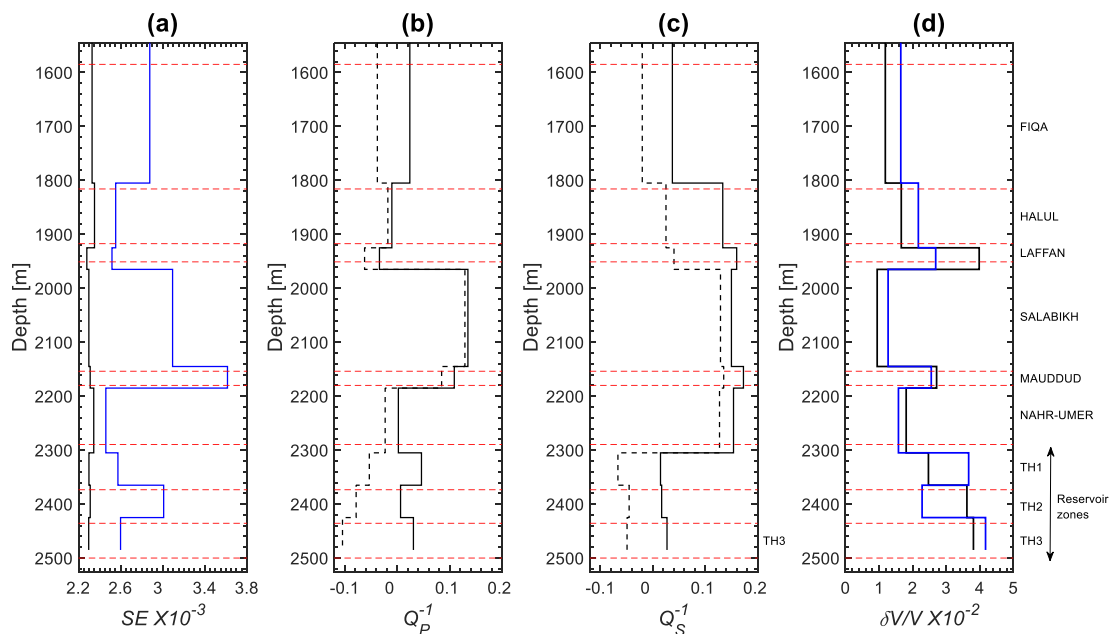
Figure 10. (a) Standard error (SE) of the linear regression of the spectral ratio versus frequency curves as a function of depth for P waves (black) and S waves (blue) in the frequency ranges 7–90 Hz and 5–85 Hz, respectively. (b) and (c) Profiles of total attenuation (solid lines) and scattering component (dashed lines) in the frequency ranges 7–90 Hz and 5–85 Hz, respectively. (d) Relative variation of the retained P (black) and S (blue) sonic velocities, which are averaged in each formation. The horizontal dashed lines and the text labels indicate the tops and names of the various formations.

A band pass filter was applied on the synthetic seismograms in order to estimate Q_{sc}^{-1} in the same frequency range used to estimate Q_P^{-1} (7–90 Hz) and Q_S^{-1} (5–85 Hz). The compressional ($Q_{\mathrm{sc}_P}^{-1}$) and shear ($Q_{\mathrm{sc}_S}^{-1}$) scattering profiles display magnitudes ranging from −0.104 to 0.123 and from −0.066 to 0.135, respectively (Figures 10b and c). Scattering magnitudes are significant, which is in agreement with the high variation of velocity with depth (Figure 10d).

Following (3), the Q_{in}^{-1} profiles were obtained after subtracting Q_{sc}^{-1} from Q profiles. The P and S intrinsic attenuation magnitudes vary from 0.009 to 0.135 and from 0.021 to 0.12, respectively (Figures 11a and b). Overall, the $Q_{\mathrm{in}_P}^{-1}$ and $Q_{\mathrm{in}_S}^{-1}$ profiles exhibit similar variation, except in Halul Formation where $Q_{\mathrm{in}_S}^{-1}$ has higher magnitude than that of $Q_{\mathrm{in}_P}^{-1}$. The highest magnitudes of $Q_{\mathrm{in}_P}^{-1}$ and $Q_{\mathrm{in}_S}^{-1}$ are noticed in the reservoir zones and Halul Formation, respectively. The magnitudes of $Q_{\mathrm{in}_P}^{-1}/Q_{\mathrm{in}_S}^{-1}$ ratio is higher than 1 in the reservoir zones, while it is less than 1 in almost all of the other shallow formations (Figure 11c). Moreover, the $Q_{\mathrm{in}_P}^{-1}/Q_{\mathrm{in}_S}^{-1}$ ratio shows a good correlation

with the resistivity profile in the reservoir zones (Figures 11d and e).

4. Estimation of sonic attenuation

Frazer et al. [1997] developed the median frequency shift (MFS) method to estimate attenuation from sonic waveforms. The MFS method is based on the following relationship between the median of frequency shift $\hat{\phi}(z)$ and the attenuation $Q^{-1}(z)$,

$$\hat{\phi}(z) = Q^{-1}(z)\Delta t(z) + \hat{A}, \qquad (5)$$

where $\Delta t(z)$ is source-receiver travel time and $\hat{A}$ is an unknown constant, which can be calculated from (5) by assuming an arbitrarily reference attenuation value $Q^{-1}(\xi)$ at a depth ξ, which yields,

$$\hat{A} = \hat{\phi}(\xi) - Q^{-1}(\xi)\Delta t(\xi) \qquad (6)$$

Hence, the values of $Q^{-1}(z)$ are relative and strongly dependent on the arbitrarily reference value $Q^{-1}(\xi)$. Suzuki and Matsushima [2013] significantly reduced the arbitrariness in $Q^{-1}(z)$ estimate, by suggesting a linear fitting of $\hat{\phi}(z)$ over $\Delta t(z)$ to define
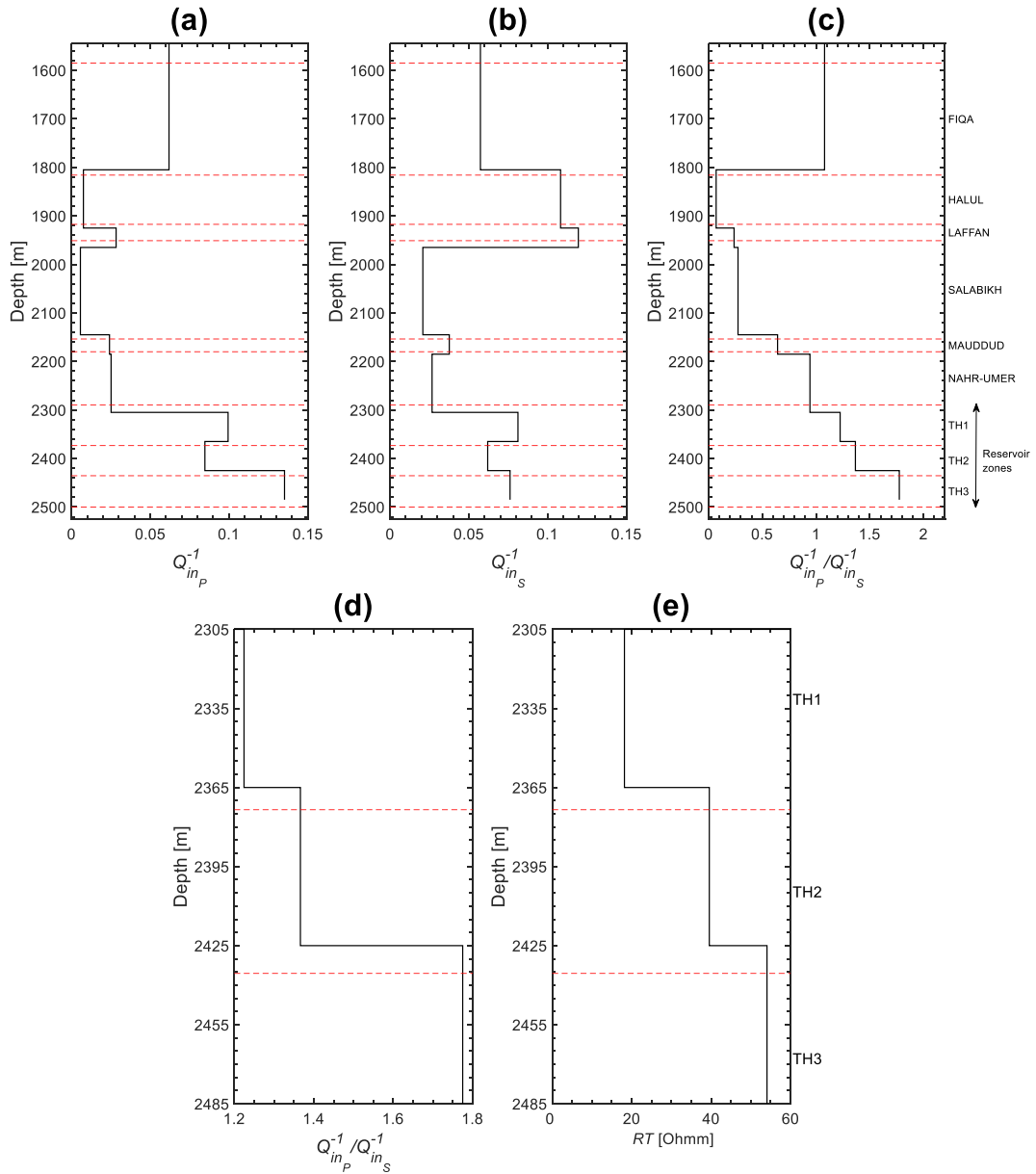
Figure 11. (a) and (b) VSP intrinsic attenuation profiles of P and S waves in the frequency ranges 7–90 Hz and 5–85 Hz, respectively. (c) P to S VSP intrinsic attenuation ratio as a function of depth. (d) P to S attenuation ratio profile in the reservoir. (e) Resistivity log averaged between receivers located at the top and the bottom of each reservoir zone. The dashed lines and the text labels indicate the tops and names of the reservoir zones.

the reference value $Q^{-1}(\xi)$. They refer to the corrected MFS method as modified mean frequency shift (MMFS) method. We use the MMFS method to estimate Q^{-1} from the sonic waveforms of this study.

Bouchaala et al. [2016a] showed that the scattering estimated in carbonate rocks at sonic frequencies is insignificant. They suggested that this might be due to the spatial sampling of sonic logging data, which is

not sufficient to catch the heterogeneities that affect sonic waves. Therefore, we consider the sonic attenuation profiles as being representative of the intrinsic attenuation. The magnitudes of compressional attenuation Q_{mo}^{-1} and shear attenuation Q_{xd}^{-1} are in the range of 0.06–0.120 and 0.034–0.085, respectively (Figures 12a and b). We notice that in the case of large (2294–2306 m) or zero (2348–2360 m and below 2370 m) clay content (Figure 12d), attenuation is relatively low while in the case of small or moderate amount of clay (2306–2348 m and 2360–2370 m) (Figure 12d), attenuation is relatively high (Figures 12a and b). As in the VSP case, the Q_{mo}^{-1}/Q_{xd}^{-1} ratio is larger than 1 (Figure 12c). The cross-plots of sonic attenuations with water content (Φ = the product of porosity and water saturation) show a clear decrease of Q_{mo}^{-1} and Q_{xd}^{-1} with increasing Φ and increase of Q_{mo}^{-1} and Q_{xd}^{-1} with increasing resistivity (Figures 13a and b).

5. Discussion

5.1. *Correlation between attenuation and petrophysical properties*

After a careful extraction of downgoing P and S waves, we were able to estimate their corresponding attenuations. The high scattering magnitudes observed in various formations (Figures 10b and c) confirm the heterogeneous nature of the oilfield's subsurface geology. This is consistent with the high variation of velocity (Figure 10d), and opposed to most attenuation studies carried out in sandstones where scattering is usually reported insignificant [e.g., Matsushima and Zhan, 2020, Pevzner et al., 2013]. However, negative magnitudes of Q_{sc}^{-1} were noticed, particularly in the reservoir zones (Figures 10b and c). Liner [2014] suggested that a negative scattering is the result of a negative impedance contrast which implies a negative normal reflection coefficient (R_0). Therefore, based on the partitioning relationship for seismic displacements $R_0 + T_0 = 1$, the normal transmission coefficient (T_0) has to be larger than 1, meaning an amplification in the amplitude of transmitted waves which results in negative Q_{sc}^{-1}. Consequently, the negative magnitudes of Q_{sc}^{-1} in the reservoir zones may be due to negative impedance variations (Figure 6) caused by high porosity and fluid content. Mateeva showed that in finely layered medium, primary reflections overlain or underlain weak reflections,

which leads to negative attenuation. Furthermore, Gist [1994] suggested that for a proper estimate of scattering, 3D heterogeneities should be taken into account. Therefore, as suggested by Bouchaala et al. [2016a], the interference of small reflections with primaries in the vicinity of receivers and the neglect of 3D heterogeneity in scattering estimation might imply negative magnitudes of Q_{sc}^{-1}.

Hassan and Azer [1985] reported a small accumulation of heavy oil in Halul Formation in the northern Abu Dhabi offshore, where the study area is located. The decrease in sonic velocities and density in the depth range of 1840–1880 m might be related to the presence of heavy oil (Figure 6). Batzle et al. [2006] pointed out the strong frequency dependence of shear modulus on heavy oil-saturated rocks, which means high shear attenuation. The relative frictional motion between solid grains and heavy oil which behaves as a solid during the wave passage due to its high viscosity might be the cause of high shear attenuation Hamilton [1972], Mavko and Nur [1979]. This is in agreement with the highest magnitude of $Q_{in_S}^{-1}$ noticed in Halul Formation, if the assumption of heavy oil content is verified. Furthermore, the highest $Q_{in_P}^{-1}$ magnitudes noticed in the reservoir zones are most probably due to fluid-related mechanisms, which mainly affect P waves.

Due to limitations in the quality of sonic waveforms, the sonic attenuation was estimated in the reservoir zone TH1 and the upper part of reservoir zone TH2 only. The notable changes of sonic attenuation with the variation of clay content (Figure 12), might be due to the effect of clay on the permeability, which controls the fluid flow and hence the intensity of attenuation mechanisms. The oil content is usually negatively correlated to water content (Φ) and directly proportional to resistivity (RT). Therefore, the clear decay of Q_{mo}^{-1} and Q_{xd}^{-1} with Φ, and their highest magnitudes at high RT areas (Figures 13a and b), suggests a good correlation with oil content. The oil trapped in this reservoir ranges from medium to light Hassan and Azer [1985]. Therefore, it behaves as a fluid during the wave passage and not as a solid as it is the case of heavy oil. Consequently, as for the VSP case, the increase of sonic attenuation with oil content is most probably due to fluid-related mechanisms, which manifest themselves through the frictional movement between pore fluids and grain solids.
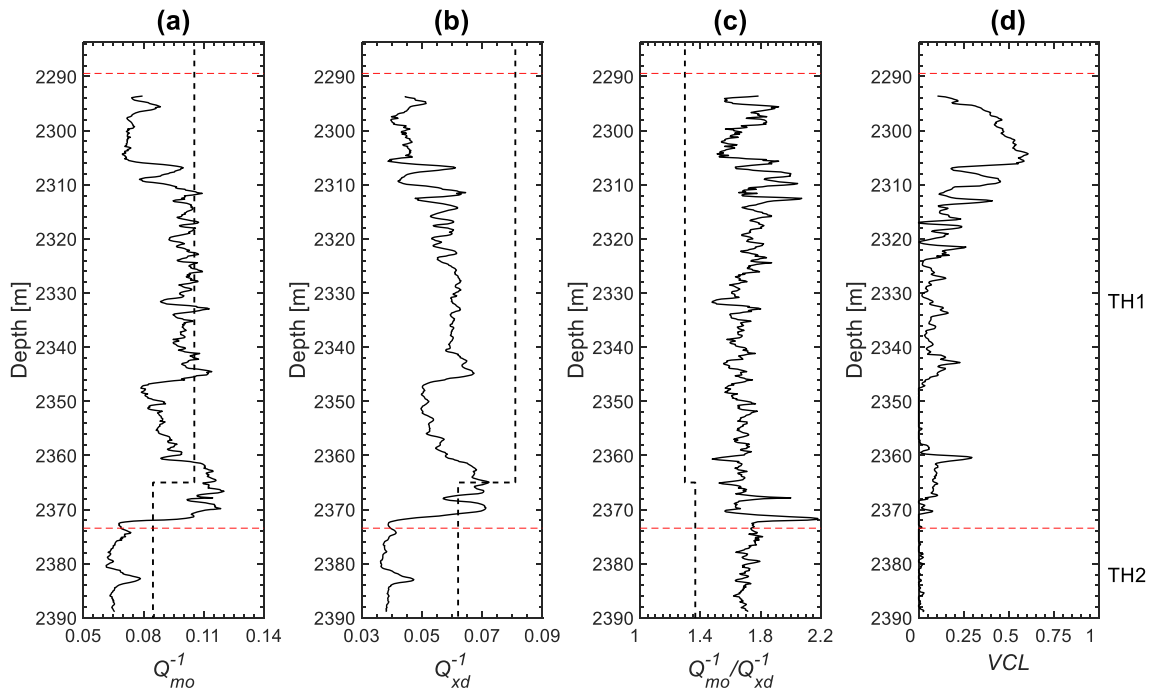
Figure 12. Attenuation profiles of (a) Monopole (compressional), (b) dipole (shear), and (c) monopole to dipole ratio (continuous curves) and their VSP counterparts (dashed lines) attenuation profiles. (d) Clay content in the reservoir zones. VCL is the fractional volume of clay. The horizontal dashed lines indicate the top and base of the reservoir TH1 zone.
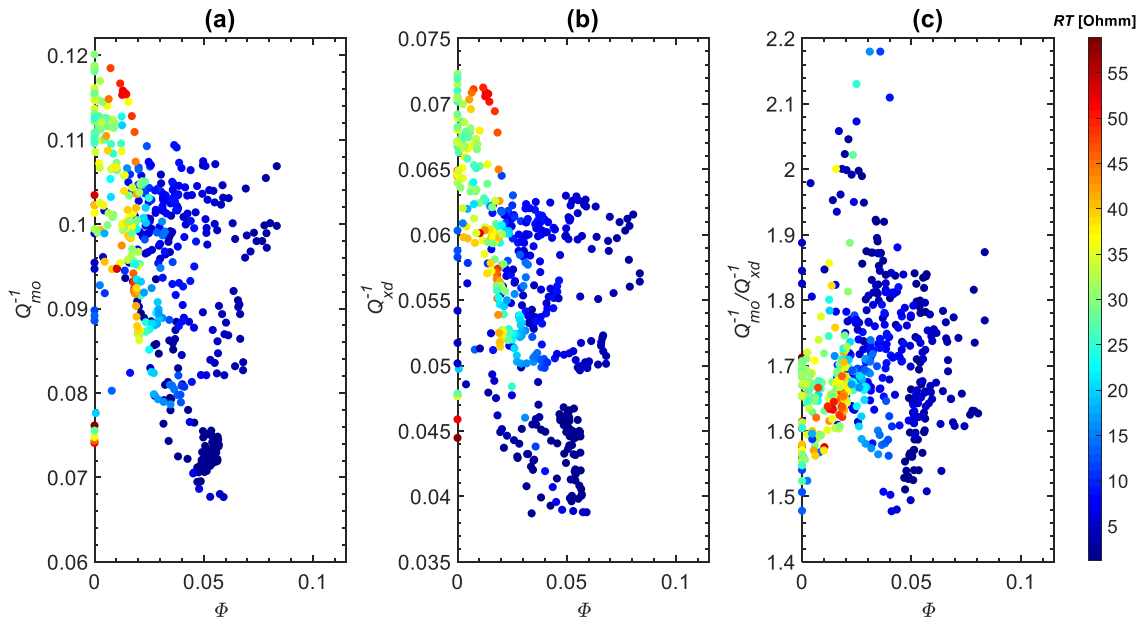

Figure 13. Cross-plots of (a) monopole, (b) dipole, and (c) monopole to dipole attenuations versus water content (Φ = porosity * water saturation), color-coded by resistivity (*RT*).

5.2. *The compressional to shear attenuation ratio in the reservoir zones*

The highest magnitudes of $Q_{\text{in}P}^{-1}/Q_{\text{in}S}^{-1}$ noticed in the reservoir zones (Figure 11c) are most likely caused by the high fluid content. As explained above for Q_{mo}^{-1} and Q_{xd}^{-1}, the good correlation between $Q_{\text{in}P}^{-1}/Q_{\text{in}S}^{-1}$ and the resistivity profiles in the reservoir zones (Figures 11d and e) suggests that the magnitude of $Q_{\text{in}P}^{-1}/Q_{\text{in}S}^{-1}$ is directly related to oil saturation. The ratio $Q_{\text{mo}}^{-1}/Q_{\text{xd}}^{-1}$ shows an increase with Poisson's ratio (ν). This increase is confirmed with two distinct models proposed by Dvorkin et al. [2014] for wet sediments, which show an increase of $Q_{\text{mo}}^{-1}/Q_{\text{xd}}^{-1}$ with ν, and which predict $Q_{\text{mo}}^{-1}/Q_{\text{xd}}^{-1}$ magnitudes between 1 and 3 in the Poisson's ratio interval 0.30–0.35 (Figure 14). However, none of the theoretical models (7) and (8) satisfactorily matches the estimated Q_P^{-1}/Q_S^{-1} value.

$$\frac{Q_P^{-1}}{Q_S^{-1}} = \frac{1}{4}\frac{\left(\frac{M}{G}-2\right)^2\left(3\frac{M}{G}-2\right)}{\left(\frac{M}{G}-1\right)\left(\frac{M}{G}\right)} \quad (7)$$

$$\frac{Q_P^{-1}}{Q_S^{-1}} = \frac{5}{4}\frac{\left(\frac{M}{G}-2\right)^2}{\left(\frac{M}{G}-1\right)} \left/ \left[\frac{2\frac{M}{G}}{\left(3\frac{M}{G}-2\right)}+\frac{\frac{M}{G}}{3\left(\frac{M}{G}-1\right)}\right], \right. \quad (8)$$

where

$$M = \rho V_P^2 \quad (9)$$
$$G = \rho V_S^2 \quad (10)$$
$$\frac{M}{G} = \frac{2-2\nu}{1-2\nu} = \frac{V_P^2}{V_S^2} \quad (11)$$

The reservoir zones, which are fully saturated with oil and water, display $Q_{\text{in}P}^{-1}/Q_{\text{in}S}^{-1}$ and $Q_{\text{mo}}^{-1}/Q_{\text{xd}}^{-1}$ magnitudes larger than 1 (Figures 11d, 12c, and 13c). This is in agreement with the observations of Adam et al. [2009] who experimentally investigated seismic wave attenuation in fully and partially saturated carbonate core plug samples acquired from one of Abu Dhabi reservoirs. However, shear attenuation is mostly observed to be greater than the compressional attenuation in fully saturated sandstones [e.g., Best et al., 1994, Murphy, 1982, Winkler and Nur, 1982]. To understand the contradiction between the two observations, it should be pointed out that the interpretation of the magnitude of compressional to shear attenuation in partially and fully saturated sandstones is based on a rock physics model assuming that fluid flows between two identical low aspect ratio cracks and orthogonal at their tips [Winkler and Nur, 1982].
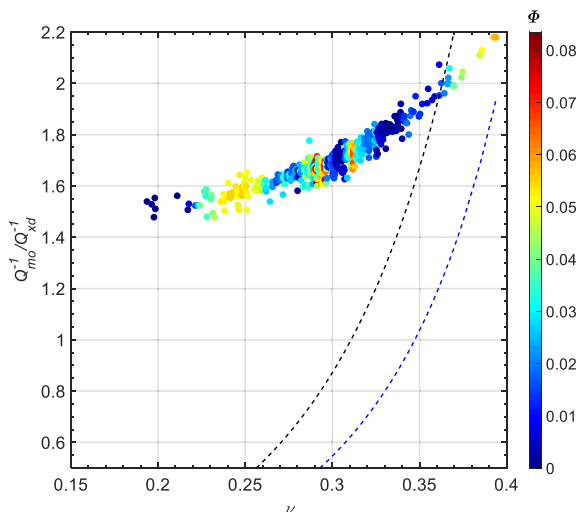

Figure 14. Cross-plot of monopole to dipole attenuation versus Poisson's ratio (ν), color-coded by water content (Φ = porosity * water saturation). The blue and black dashed curves were produced from (7) and (8), respectively.

This conceptual model is too simple and not adequate for carbonate rocks known for their complex texture. Therefore, the degree of fluid saturation is not the unique parameter which controls the magnitude of attenuation ratio in carbonate rocks.

5.3. *Frequency dependence and attenuation mechanisms*

The attenuation magnitudes at sonic and VSP frequencies are of the same order (Figures 11a, b, 12a and b). This suggests frequency-independent attenuations in this oilfield. Moreover, compressional and shear attenuations show similar variation in both frequency ranges (Figures 12a and b). The positive correlation of attenuation magnitudes with resistivity and its negative correlation with water content, implies a positive correlation between attenuation and oil. Therefore, we suggest that the fluid-related mechanisms such as global and squirt flow mechanisms [e.g., Müller et al., 2010, Murphy et al., 1986] caused by the oil at VSP frequencies, induce a higher increase in the compressional attenuation than in the shear attenuation. Klimentos [1995] assumes that during the wave passage, the compliant pores located between clay (soft material) face higher deformation

than stiff pores located between carbonate grains (hard material), which results in the squeezing of the fluid contained in compliant pores. Consequently, the fluid flows toward stiff pores with high speed, which causes high frictional losses known as by the squirt flow mechanism. Accordingly, squirt flow mechanism is weak in media with very low amount of clay or with high amount of clay. This may explain the higher sonic attenuation in the zone with moderate clay content than the zones with high or no clay content (Figure 12).

6. Conclusions

We investigated the link between petrophysical properties of carbonate rocks and attenuation estimated from downgoing P and S waveforms carefully extracted from 3D VSP and sonic data. The elevated magnitudes of scattering at VSP frequencies confirms the highly heterogeneous and complex nature of carbonate rocks. The high magnitudes of $Q_{in_P}^{-1}$ and $Q_{in_P}^{-1}/Q_{in_S}^{-1}$ ratio indicate oil-rich zones, while high shear attenuation indicates a heavy oil zone. At sonic scale, both Q_{mo}^{-1} and Q_{xd}^{-1} show high sensitivity to oil content through their high magnitudes in high resistivity and low water content zones. Furthermore, clay content also controls the magnitude of attenuation through squirt flow mechanism, which is strong at moderate amount of clay. The higher than 1 magnitude of compressional to shear attenuations in the reservoir zones confirms the previous experimental results carried out on fully saturated carbonate samples, and suggests the non-validity of sandstones attenuation models for carbonate rocks.

Acknowledgment

Appendix A. The wavefield separation method, Wavesip [Leaney, 2002]

This technique is applied on 3C VSP data rotated to the geographical coordinate system (Easting, Northing, and Vertical). The data are then converted to the frequency domain by applying the Fourier
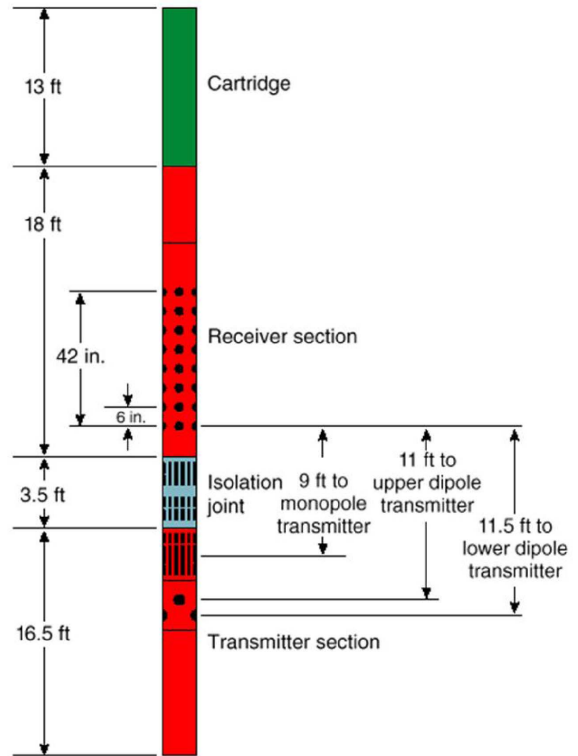

Figure 15. Illustration of Dipole Sonic Imager (DSI) tool, used to acquire the sonic data.

transform in order to obtain the linear system below at each frequency,

$$\mathbf{Gm} = \mathbf{d}, \tag{A1}$$

where **G** is the polarization-moveout matrix, $\mathbf{m} = (a_1, a_2, \ldots, a_N)$ is a vector containing the unknown amplitudes of a set of N plane waves, and **d** is the vector of 3C data in the geographical coordinate system.

For an array of M 3C geophones, the matrix **G** has N columns and $3M$ rows, each element of the matrix is written as $P_{n_i}e^{i\omega(S_n \cdot D_m)}$, where $P_{n_{i(i=1,2,3)}}$ is a component of the polarization vector and S_n is the slowness vector of each plane-wave n (qP, qSv, or Sh), respectively, and D_m is the coordinate of the mth receiver in the geographical system.

Slowness and polarization vectors are computed for each plane wave to solve the linear system in (A1), at each frequency to yield the plane-wave amplitudes and hence, to decompose the data into an angular spectrum of plane waves. In our case, the five parameter inversion simplex method [Leaney, 2000]
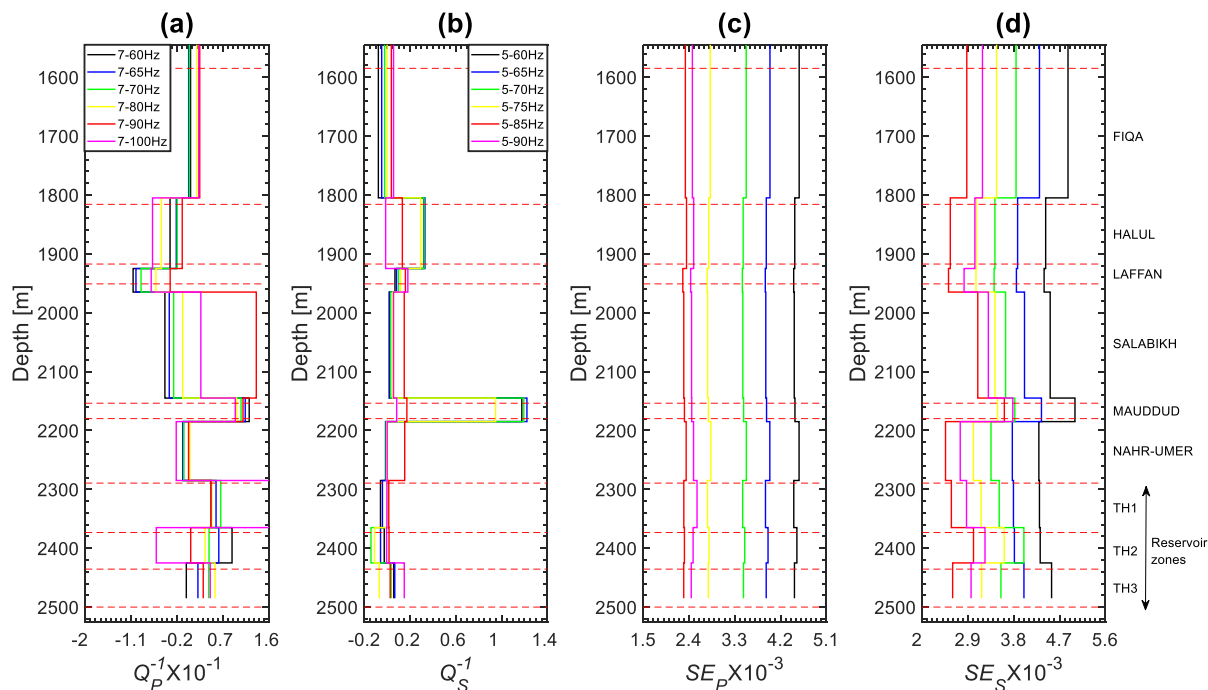
Figure 16. VSP attenuation profiles of (a) P waves and (b) S waves as function of depth estimated in different frequency ranges and their corresponding standard errors (c and d).

was used to estimate qP and qSv slowness and polarization. Eventually, the decomposed plane waves are summed by type into downgoing qP, upgoing qP, downgoing qSv, and upgoing qSv wavefields.

References

Adam, L., Batzle, M., Lewallen, K., and van Wijk, K. (2009). Seismic wave attenuation in carbonates. *J. Geophys. Res. Solid Earth*, 114(B6), 1–14.

Ali, M. Y. and Farid, A. (2016). Cretaceous–Neogene structural evolution of SE Abu Dhabi, United Arab Emirates. *J. Pet. Geol.*, 39(3), 221–245.

Armstrong, P. N. (2005). *Method of Estimating Relative Bearing of a Borehole Receiver*. Patent and Trademark Office, Washington, DC, USA.

Assefa, S., McCann, C., and Sothcott, J. (1999). Attenuation of P- and S-waves in limestones. *Geophys. Prospect.*, 47(3), 359–392.

Bath, M. (1974). *Spectral Analysis in Geophysics.* Elsevier Science, Amsterdam.

Batzle, M., Hofmann, R., and Han, D. (2006). Heavy oils—seismic properties. *Lead. Edge*, 25(6), 750–756.

Best, A., McCann, C., and Sothcott, J. (1994). The relationships between the velocities, attenuations and petrophysical properties of reservoir sedimentary rocks 1. *Geophys. Prospect.*, 42(2), 151–178.

Boadu, F. K. (1997). Rock properties and seismic attenuation: neural network analysis. *Pure Appl. Geophys.*, 149(3), 507–524.

Bouchaala, F., Ali, M. Y., and Farid, A. (2014). Estimation of compressional seismic wave attenuation of carbonate rocks in Abu Dhabi, United Arab Emirates. *C. R. Geosci.*, 346(7–8), 169–178.

Bouchaala, F., Ali, M. Y., and Matsushima, J. (2016a). Attenuation modes from vertical seismic profiling and sonic waveform in a carbonate reservoir, Abu Dhabi, United Arab Emirates. *Geophys. Prospect.*, 64, 1030–1047. Advances in Rock Physics.

Bouchaala, F., Ali, M. Y., and Matsushima, J. (2016b). Estimation of seismic attenuation in carbonate rocks using three different methods: application on VSP data from Abu Dhabi oilfield. *J. Appl. Geophys.*, 129, 79–91.

Bouchaala, F., Ali, M. Y., Matsushima, J., Bouzidi, Y., Takam Takougang, E. M., Mohamed, A. A., and Sul-

tan, A. (2019b). Azimuthal investigation of compressional seismic-wave attenuation in a fractured reservoir. *Geophysics*, 84(6), B437–B446.

Bouchaala, F., Ali, M. Y., Matsushima, J., Bouzidi, Y., Takougang, E. T., Mohamed, A. A., and Sultan, A. A. (2019a). Scattering and intrinsic attenuation as a potential tool for studying of a fractured reservoir. *J. Pet. Sci. Eng.*, 174, 533–543.

Bouchaala, F. and Guennou, C. (2012). Estimation of viscoelastic attenuation of real seismic data by use of ray tracing software: Application to the detection of gas hydrates and free gas. *C. R. Geosci.*, 344(2), 57–66.

Del Pezzo, E., Giampiccolo, E., Tuvè, T., Di Grazia, G., Gresta, S., and Ibàñez, J. M. (2019). Study of the regional pattern of intrinsic and scattering seismic attenuation in Eastern Sicily (Italy) from local earthquakes. *Geophys. J. Int.*, 218(2), 1456–1468.

Dvorkin, J., Gutierrez, M. A., and Grana, D. (2014). *Seismic Reflections of Rock Properties*. Cambridge University Press, Cambridge.

Edwards, H. E., Sit, K. H., Bu-Al-Rougha, H., Sultan, A. A., and Khouri, N. (2006). Tectonic history and basement fault control on structural development of an offshore field, Abu Dhabi. In *Abu Dhabi International Petroleum Exhibition and Conference*. Society of Petroleum Engineers.

Frazer, L. N., Sun, X., and Wilkens, R. H. (1997). Changes in attenuation with depth in an ocean carbonate section: Ocean Drilling Program sites 806 and 807, Ontong Java Plateau. *J. Geophys. Res. Solid Earth*, 102(B2), 2983–2997.

Gist, G. A. (1994). Seismic attenuation from 3-D heterogeneities: a possible resolution of the VSP attenuation paradox. In *SEG Technical Program Expanded Abstracts 1994*, pages 1042–1045. Society of Exploration Geophysicists.

Goupillaud, P. L. (1961). An approach to inverse filtering of near-surface layer effects from seismic records. *Geophysics*, 26(6), 754–760.

Graves, J., Checkles, S., Leveille, J., Campbell, A., Deri, C. P., and Leaney, S. (2008). 3D VSP acquisition and 3C processing on a deep subsalt prospect in the Gulf of Mexico. In *SEG Annual Meeting, Las Vegas, Nevada, USA*.

Guo, J. and Lin, D. (2003). High-amplitude noise attenuation. In *SEG Technical Program Expanded Abstracts 2003*, pages 1893–1896. Society of Exploration Geophysicists, Dallas, Texas, USA.

Hamilton, E. L. (1972). Compressional-wave attenuation in marine sediments. *Geophysics*, 37(4), 620–646.

Hassan, T. and Azer, S. (1985). The occurrence and origin of oil in offshore Abu Dhabi. In *Middle East Oil Technical Conference and Exhibition*, Manama, Bahrain. Society of Petroleum Engineers.

Kazemi, K. and Naville, C. (2017). Orientation method applied to onshore 3-component VSP's recorded with a relative bearing sensor in partially low deviated boreholes. In *Fourth EAGE Borehole Geophysics Workshop*, pages 1–5, Abu Dhabi, UAE. European Association of Geoscientists & Engineers.

Klimentos, T. (1995). Attenuation of P-and S-waves as a method of distinguishing gas and condensate from oil and water. *Geophysics*, 60(2), 447–458.

Leaney, W. S. (2000). Look-ahead walkaways using effective VTI models. In *SEG Technical Program Expanded Abstracts 2000*, pages 1743–1747. Society of Exploration Geophysicists, Calgary, Alberta, Canada.

Leaney, W. S. (2002). Anisotropic vector plane wave decomposition for 3D VSP data. In *SEG Technical Program Expanded Abstracts 2002*, pages 2369–2372. Society of Exploration Geophysicists, Salt Lake City, Utah, USA.

Li, F., Huang, L., Zhang, H., and Yang, T. (2018). Attenuation of acoustic emission propagation along a steel strand embedded in concrete. *KSCE J. Civ. Eng.*, 22(1), 222–230.

Liner, C. L. (2014). Long-wave elastic attenuation produced by horizontal layering. *Lead. Edge*, 33(6), 634–638.

Matsushima, J., Ali, M. Y., and Bouchaala, F. (2018). Attenuation estimation from sonic logging waveforms combining seismic interferometry and common-midpoint approach. *Geophysics*, 83(1), WA21–WA35.

Matsushima, J. and Zhan, L. (2020). S-wave attenuation estimation from walkaway vertical seismic profiling data in methane hydrate-bearing sediments at Nankai Trough, Japan. *J. Appl. Geophys.*, 173, article no. 103931.

Mavko, G. M. and Nur, A. (1979). Wave attenuation in partially saturated rocks. *Geophysics*, 44(2), 161–178.

McDonal, F., Angona, F., Mills, R., Sengbush, R., Van Nostrand, R., and White, J. (1958). Attenuation

of shear and compressional waves in Pierre shale. *Geophysics*, 23(3), 421–439.

Müller, T. M., Gurevich, B., and Lebedev, M. (2010). Seismic wave attenuation and dispersion resulting from wave-induced flow in porous rocks—A review. *Geophysics*, 75(5), 75A147–75A164.

Murphy, W. F. (1982). Effects of partial water saturation on attenuation in Massilon sandstone and Vycor porous glass. *J. Acoust. Soc. Am.*, 71(6), 1458–1468.

Murphy, W. F., Winkler, K. W., and Kleinberg, R. L. (1986). Acoustic relaxation in sedimentary rocks: Dependence on grain contacts and fluid saturation. *Geophysics*, 51(3), 757–766.

Pevzner, R., Muller, T., Galvin, R., Alasbali, A., Urosevic, M., and Gurevich, B. (2013). Seismic attenuation from VSP and well log data: approaches, problems and relative contribution of scattering. In *EAGE Workshop on Seismic Attenuation*, Singapore. European Association of Geoscientists & Engineers. cp-363–00009.

Prudencio, J., Del Pezzo, E., García-Yeguas, A., and Ibáñez, J. M. (2013). Spatial distribution of intrinsic and scattering seismic attenuation in active volcanic islands–I: model and the case of Tenerife Island. *Geophys. J. Int.*, 195(3), 1942–1956.

Qi, Q., Müller, T. M., and Pervukhina, M. (2017). Sonic QP/QS ratio as diagnostic tool for shale gas saturation. *Geophysics*, 82(3), MR97–MR103.

Schoenberger, M. and Levin, F. (1974). Apparent attenuation due to intrabed multiples. *Geophysics*, 39(3), 278–291.

Shabelansky, A. H., Malcolm, A., and Fehler, M. (2015). Monitoring viscosity changes from time-lapse seismic attenuation: case study from a heavy oil reservoir. *Geophys. Prospect.*, 63(5), 1070–1085.

Shekhar, R., Naqbi, A. A., Obeta, C., Ottinger, G., Herrmann, R., Obara, T., Almazrouei, S. J., Maqrami, Z. N. A., Neyadi, A. A., and Edwards, E. (2017). Implementation of high resolution diagenetic features into the static and dynamic reservoir models of a Giant Offshore Oil Field, Abu Dhabi. In *Abu Dhabi International Petroleum Exhibition and Conference*, Abu Dhabi, UAE. Society of Petroleum Engineers.

Skeith, G., Obara, T., El-Awawdeh, R., Sultan, A., Al Messabi, A., Liu, E., Johns, M., Zelewski, G., Burnett, W., and Wu, X. (2015). Improved fracture characterization by utilizing seismic-derived attributes including anisotropy and diffraction imaging in a Giant offshore Carbonate Field, UAE. In *Abu Dhabi International Petroleum Exhibition and Conference*, Abu Dhabi, UAE. Society of Petroleum Engineers.

Suzuki, H. and Matsushima, J. (2013). Quantifying uncertainties in attenuation estimation at methane-hydrate-bearing zones using sonic waveform logs. *Geophysics*, 78(5), D339–D353.

Takougang, E. M. T., Ali, M. Y., Bouzidi, Y., Bouchaala, F., Sultan, A. A., and Mohamed, A. I. (2020). Characterization of a carbonate reservoir using elastic full-waveform inversion of vertical seismic profile data. *Geophys. Prospect.*, 68(6), 1944–1957.

Winkler, K. W. and Nur, A. (1982). Seismic attenuation: Effects of pore fluids and frictional-sliding. *Geophysics*, 47(1), 1–15.

Wu, R.-S. and Aki, K. (1988). Introduction: Seismic wave scattering in three-dimensionally heterogeneous earth. In *Scattering and Attenuations of Seismic Waves, Part I*, pages 1–6. Springer, Basel, Switzerland.

Wu, X., Yuan, Y., and Li, H. (2017). Anomalous amplitudes attenuation based on the seismic wave propagation theory. In *International Geophysical Conference, Qingdao, China, 17–20 April 2017*, pages 365–368, Qingdao, China. Society of Exploration Geophysicists and Chinese Petroleum Society.